HHS Public Access

Author manuscript

Magn Reson Med. Author manuscript; available in PMC 2015 April 22.

Published in final edited form as:

Magn Reson Med. 2008 February ; 59(2): 396–409. doi:10.1002/mrm.21476.

Local B_1^+ Shimming for Prostate Imaging with Transceiver Arrays at 7T Based on Subject-Dependent Transmit Phase Measurements

Gregory J. Metzger[1,*], **Carl Snyder**[1], **Can Akgun**[1], **Tommy Vaughan**[1], **Kamil Ugurbil**[1,2], and **Pierre-Francois Van de Moortele**[1]

[1]Center for Magnetic Resonance Research, Department of Radiology, University of Minnesota Medical School, Minneapolis, Minnesota

[2]Max Plank Institut für Biologische Kybernetic, Hochfeld-Magnetresonanz-Zentrum, Tübingen, Germany

Abstract

High-quality prostate images were obtained with transceiver arrays at 7T after performing subject-dependent local transmit B_1 (B_1^+) shimming to minimize B_1^+ losses resulting from destructive interferences. B_1^+ shimming was performed by altering the input phase of individual RF channels based on relative B_1^+ phase maps rapidly obtained in vivo for each channel of an eight-element stripline coil. The relative transmit phases needed to maximize B_1^+ coherence within a limited region around the prostate greatly differed from those dictated by coil geometry and were highly subject-dependent. A set of transmit phases determined by B_1^+ shimming provided a gain in transmit efficiency of 4.2 ± 2.7 in the prostate when compared to the standard transmit phases determined by coil geometry. This increased efficiency resulted in large reductions in required RF power for a given flip angle in the prostate which, when accounted for in modeling studies, resulted in significant reductions of local specific absorption rates. Additionally, B_1^+ shimming decreased B_1^+ nonuniformity within the prostate from (24 ± 9%) to (5 ± 4%). This study demonstrates the tremendous impact of fast local B_1^+ phase shimming on ultrahigh magnetic field body imaging.

Keywords

prostate; B_1^+ shimming; 7T; stripline array; transmit array; transceive array; FDTD model; SAR

The use of high magnetic fields can improve our ability to investigate the etiology and development of prostate cancer. Gains may also be expected in diagnosis, treatment monitoring, and in the development of new therapies. Improved diagnosis of extracapsular extension through T_2w anatomic imaging has been reported, while greater benefits were anticipated for spectroscopy and dynamic contrast-enhanced imaging when progressing

[*]Correspondence to: Greg Metzger, PhD, Center for Magnetic Resonance Research, University of Minnesota, 2021 6th St. S.E., Minneapolis, MN 55455. gmetzger@umn.edu.

from 1.5–3.0T (1). Using even higher magnetic fields can bring further benefits by exploiting the advantages of increased signal-to-noise ratio (SNR) (2), spectral resolution (3), and parallel imaging performance (4). However, imaging the human body at the ultrahigh magnetic field (UHF) of 7T is very challenging. As a result, virtually all MRI and MRS studies that have been reported so far in humans at UHF have focused on the brain; only recently, efforts from our laboratory have demonstrated that human torso imaging may also be feasible at UHF (5–7).

Arguably, the most difficult challenges encountered at UHF are due to strong transmit B_1 (B_1^+) field heterogeneities in large biological samples. As the RF wavelength used in MR approaches or becomes shorter than the dimensions of the object to be imaged, significant B_1^+ field distortions occur that are dependent on tissue electromagnetic properties and geometry (8,9). At 7T the RF wavelength in biological tissues at the Larmor frequency (≈300 MHz) is ≈12 cm on average; these rather short wavelengths result in complex transmit and receive B_1 profiles in human tissues (10,11). However, the consequences are dramatically different, first, between receive and transmit B_1 fields, and second, between surface and volume RF coils.

On the receive side the use of multiple coils with independent receive channels for data sampling are now available on most clinical scanners. By correctly combining the data from these multiple receivers it is possible to avoid destructive interferences between receive B_1 fields (B_1^-), resulting in optimized SNR in the reconstructed images. On the transmit side, single surface coils can still be utilized at UHF in ways similar to those at lower field, sharing with the latter a stronger B_1^+ field magnitude within the vicinity of the RF coil. However, the B_1^+ profiles of volume RF coils at UHF exhibit higher magnitude in the center than in the periphery (2), a feature often described as a “bright center.” This is the result of a complicated combination of destructive and constructive interferences, dielectric phenomenon, and damping wave patterns (10–14).

It had been shown by Vaughan et al. (15) that a more homogeneous B_1^+ field can be obtained by adjusting individual current-carrying elements within a volume coil at high field, but the adjustments needed for this B_1^+ shimming (also referred to as RF shimming or field focusing) approach are not trivial and depend on both a given subject’s anatomy and the positioning of the coil. More recently, a strong interest has developed in utilizing multiple, independent transmit RF coils to cover a volume rather than a traditional one-channel transmit volume coil (16,17). Such coil designs allow for more flexible B_1^+ shimming approaches by potentially modulating the phase and/or magnitude of each transmit element in an array (9,18), a property that becomes far more critical at 7T and higher fields (19–21).

When B_1^+ shimming is considered at UHF with a transmit coil array, it is essential to appreciate two different sources of transmit B_1^+ heterogeneity. One source is the intrinsically distorted B_1^+ pattern of each transmitting coil element observed at high field with lossy dielectric biological tissues. Such a distorted B_1^+ pattern obtained with a single coil element cannot be altered for a given coil and sample geometry, except if electromagnetic properties of the surrounding media are altered, as was demonstrated with

dielectric padding (22). Another source, however, results from *interactions* between the individual complex B_1^+ patterns from each coil element. Indeed, the volume excitation pattern of a transmit coil array corresponds to the linear combination of each individual coil's complex B_1^+ maps, the constructive or destructive nature of which being defined by the local relative phases of each transmit B_1^+ field: constructive when relative B_1^+ phases are coherent, destructive when they are incoherent.

It has been demonstrated at 7T that the complex and distorted nature of relative B_1^+ phase patterns within an array of transmit coils is responsible for large and spatially nonuniform destructive B_1^+ interferences (12). The presence of these destructive interferences results in two major, direct consequences with implications for transmit array coils at very high fields in humans. First, the sum of any set of B_1^+ phases and magnitudes will produce in some spatial locations significant losses in combined B_1^+ magnitude compared with the direct sum of all B_1^+ magnitudes in the same location. Second, because B_1^+ profiles vary relatively slowly through space, it is possible to avoid most of B_1^+ cancellation within any chosen, relatively small, region of interest (ROI) by setting the average local B_1^+ phase of each transmit coil to an identical value (12,21). The principle of controlling transmit phases (18,19) or transmit phases *and* amplitudes (9) with multiple independent transmit channels in order to alter B_1^+ profiles in humans has been previously demonstrated. However, the experimental adjustments described in most of those studies were empirically obtained by iteratively trying different sets of phase and/or magnitude over multiple coils and estimating the results with image comparisons.

In the present study we demonstrate a fast, local B_1^+ shimming approach based on subject-dependent calibration data to obtain B_1^+ phase coherence within a limited ROI (21) drawn around the prostate. This method is demonstrated to produce significant increases in local B_1^+ magnitude for a given RF power input, resulting in a decrease of the required RF power levels. Furthermore, B_1^+ becomes more homogeneous within the ROI, yielding greatly improved image quality with more uniform contrast. We report significant variations in relative transmit phases between coil elements from subject to subject, even when utilizing the same transmit RF coil array. These results emphasize the importance of *measuring* the relative B_1^+ phases at UHF (12), rather than iteratively trying different sets of phases (18) in order to perform local B_1^+ shimming. The methods presented should facilitate the development of clinical MR spectroscopy and imaging investigations at UHF, not only in the prostate (23) but also in a variety of organs (e.g., heart or brain) when a local B_1^+ adjustment is needed and sufficient (24).

In contrast to B_1^+ shimming methods that include channel-dependent transmit amplitude optimization, the local phase-based approach has several advantages. First, local B_1^+ phase shimming does not require the absolute mapping of B_1^+ magnitude for each transmit channel. While rapid B_1^+ mapping strategies are under active development, acquiring these data for multiple transmit coil elements is still not trivial. Another important consideration concerns the simplicity of the hardware required for local B_1^+ phase shimming that can be performed with a single transmit channel through the means of commercially available high-power RF splitters and phase shifters, as demonstrated in the present study. This is standard hardware for most UHF sites and therefore makes the proposed methods practical, and in

cases focusing on small ROIs, completely sufficient. On the contrary, methods employing amplitude adjustments require the use of multiple independent RF amplifiers and associated safety monitoring. While this is a rapidly expanding area of development, only a few centers currently have the required hardware to perform this type of optimization in vivo. In addition, where a single transmit channel setup can utilize the RF power monitoring interface existing on standard consoles, significant hardware and software modifications are required to ensure RF safety for in vivo applications on systems with multiple independent transmitters. Optimizing transmit RF amplitudes, additionally to transmit RF phases, typically becomes desirable when a primary goal is to improve transmit B_1^+ homogeneity over a certain ROI. However, it is demonstrated in this article that for the prostate, which is an organ of limited size and approximately centered in the body along the XY plane, optimizing the effective local B_1^+ magnitude based solely on a local B_1^+ phase results in high B_1^+ homogeneity within the prostate.

MATERIALS AND METHODS

In vivo data were acquired on volunteers with signed consent under an Institutional Review Board-approved protocol. The MRI system used for this study included a Magnex 7T, 90-cm bore magnet with Siemens console, whole body gradients, and 16 independent RF receivers. A single 8 kW RF amplifier (CPC, Brentwood, NY) was utilized for transmission. The RF power was split with equal amplitude through an eight-way splitter (Werlatone, Brewster, NY) with −0.4 dB insertion loss per path and ±1° phase shift. Each of the eight RF outputs were directed toward custom-built Transmit/Receive (T/R) switches allowing for both transmit and receive operations. For each transmit channel a phase shifter (ATM Microwave, Patchogue, NY) was inserted between the eight-way splitter and the corresponding T/R switch, allowing for an adjustable phase range from 0° to 108° for every channel (the eight-phase shifters were calibrated for 300 MHz operation). Phase shifts larger than 108° were obtained with additional RF cables of different lengths (fine phase tuning was obtained with the phase shifters). B_1^+ mapping and B_1^+ shimming calculation were performed in IDL (ITT Visual Information Solutions, Boulder, CO) and Matlab (MathWorks, Natick, MA). All acquisitions complied with FDA guidelines for specific absorption rates (SAR) and gradient duty cycle.

Coil Design

Two similar eight-channel flexible transceiver array coils, referred to in Table 1 as coils 1 and 2, were built according to stripline transmission line principles (19,25). The individual coil elements were 15.3 cm in length with a 1.27 cm inner conductor width and a 5.0 cm outer conductor width. For coil 1, an air gap of 1.3 cm separated each coil element while a 1.3 cm thick polytetrafluoroethylene (PTFE) dielectric with a low loss tangent and a permittivity of 2.08 separated the inner and outer conductor. For coil 2, a 4.3 cm air gap separated each coil element while the dielectric thickness between the inner and outer conductor was 1.9 cm. Each element was individually tuned to proton's resonant frequency at 7T and matched to a nominal 50Ω line. Capacitive decoupling allowed for more than −15 dB of isolation between nearest-neighbor elements when loaded and −18 dB when unloaded (26). Two identical PTFE plates (22.7 × 5.6 cm) were built to secure and house four coil

elements resulting in a four-channel anterior and four-channel posterior array. The plates were only 0.3 cm thick; this provided a flexible former that allowed both arrays for a given coil to be contoured to individual subjects. The ground side of the anterior array was covered with 1 cm of closed cell foam to prevent any contact of the electrical components by the subject. All bench measurements were performed using a calibrated Hewlett-Packard (Palo Alto, CA) HP 4396A network analyzer together with an 85046A "S" parameter test set. The anterior four-channel array for coil 2 is shown in Fig. 1a.

The relative positions of the eight coil elements are shown schematically in Fig. 1b, along with phases dictated by coil geometry for the two coil configurations. These phases were derived by the azimuthal position of each element given a focal region of interest at the center assuming the anterior and posterior plates were 20 cm apart. The phases dictated by coil geometry that are listed in Fig. 1b are also provided in Table 1, along with the subject-dependent phases calculated by the B_1^+ shimming methods described below.

MR Protocol

Imaging studies were performed on eight volunteers and consisted of multiplanar gradient echo (GRE) scout images, anatomic GRE, and turbo spin echo (TSE) images, along with B_1^+ shimming and B_1^+ mapping acquisitions. Other than the scout acquisition, all sequences were acquired both before and after calculation and implementation of the subject-dependent phase corrections determined by the local B_1^+ shimming procedure. The transverse GE anatomic images were acquired with the following parameters: acquisition matrix = 320 × 320, field of view (FOV) of 34 cm, a nominal flip angle of 10°, 5 mm slice thickness, and repetition time (TR) and echo time (TE) of 40 ms and 3.68 ms, respectively. It should be noted that the nominal flip angles as prescribed on the console are not expected to correspond to the actual flip angle obtained in the prostate because the average RF calibration performed by the system does not account for the distorted B_1^+ field as previously described by Collins and Smith (27).

The transverse TSE acquisition was a respiratory triggered sequence with a 100 – 400 ms delay after a system determined end-expiration. Respiration was monitored with a bellows system positioned under the anterior surface of the imaging coil which transmitted a continuous signal via Bluetooth to a receiver inside the scanner room. The TSE images were acquired with a nominal refocusing pulse of 120° or 150° and an echo train length of 13, scan matrix of 256, 220 mm FOV, 5 mm slice thickness, and TE = 102 ms.

Relative B_1^+ Phase Mapping

For each subject a series of low-resolution, low flip angle GRE images were acquired when pulsing the RF power through only one coil at a time, while the receive signal was always sampled on all eight receive channels. For each of these acquisitions, RF cables were rewired in order to temporarily direct the RF power through a single channel, each time with an identical RF cable length (thus with identical input RF phase), bypassing for this single transmitting channel the eight-way splitter and the phase shifters. This procedure was repeated until data were obtained for each of the eight transmit channels. The acquisition parameters were: FOV = 300 –320 mm, TR = 100 ms, TE = 4.1 ms, acquisition matrix =

128 × 128, 1–2 averages, and a 10 mm slice thickness. A low, identical level of RF power was utilized for each image with a single transmitting coil, providing a flip angle of less than 10° within the prostate. The relative transmit B_1^+ phases were then calculated using the B_1^+ phase formalism introduced by Van de Moortele et al. (12). As suggested by the preliminary results at 9.4T in the head, this formalism can be utilized to perform B_1^+ shimming (21). A detailed description of the methods used in this study follows.

Consider an RF coil system with M transmit elements and N receive elements. For the transceiver array demonstrated in Fig. 1b, M is equal to N, but this algorithm is applicable to coil systems with separate transmit and receive elements where $M \neq N$. The input data is generated by the GRE sequence described above while transmitting through a single coil element and receiving on all N elements. This is repeated a total of M times, one for each transmit channel, producing a set of complex images:

$$\hat{\mathbf{p}}_{j,k} = \mathbf{A}_{j,k} \cdot e^{i\varphi_{j,k}},$$

where j is the index of the receive channel (j=1,2,…, N), k is the index of the transmit channel (k=1,2,…, M), $\mathbf{A}_{j,k}$ is the measured magnitude image and $\boldsymbol{\phi}_{j,k}$ is the phase image. By arbitrarily selecting the first transmit channel (k=1) as the transmit phase reference and ignoring the magnitude information, $\mathbf{A}_{j,k}$, the relative transmit phase map for each transmit channel, k, was calculated by:

$$\Psi_k = \arg\left(\sum_{j=1}^{N}\left(e^{i\varphi_{j,k}}e^{-i\varphi_{j,l}}\right)\right), \quad [1]$$

where Ψ_k is the relative transmit phase map for each transmit channel (see Appendix). Note that dividing by the reference channel data, $e^{i\varphi j,l}$, removes all receive B_1 (B_1^-) phase contributions prior to summing over the receive channels, j, for each Ψ_k. Moreover, summing over the receive channels increases SNR in the relative transmit phase maps.

Local B_1^+ Phase Shimming

Local B_1^+ phase shimming is performed by determining a set of transmit phases that will maximize the B_1^+ phase coherence within an ROI graphically prescribed in a custom GUI written in Matlab. These phases are calculated by averaging the relative transmit phase from Eq. [1] over the chosen ROI,

$$\alpha_k = \arg\left(\sum_{ROI} e^{i\psi_k}\right). \quad [2]$$

We will refer to such set of phases α_k (k=1,2,…, M) as "B_1^+ shim phases." B_1^+ shimming is performed by subtracting these phases from each transmit channel (through the means of phase shifters and RF cable lengths) for subsequent acquisitions when transmitting with all channels simultaneously. Note that the B_1^+ shimming method described here does not attempt to create a homogeneous transmit B_1^+ over the ROI, rather it minimizes destructive

interferences within the ROI between complex $B_{1,k}^{+}$ fields of multiple transmit elements, thus maximizing the available B_1^+ magnitude.

Available B_1^+ Fraction

In any location the theoretical maximum efficiency of a transmit coil array occurs with complete phase coherence between all transmit $B_{1,k}^{+}$ vectors. In such a case, the magnitude of the sum (MOS) of the complex $B_{1,k}^{+}$ vectors equals the sum of their magnitude (SOM) where the fraction of available B_1^+, defined here as the ratio $\mathrm{MOS}(B_{1,k}^{+})/\mathrm{SOM}(B_{1,k}^{+})$, is equal to 1.0. This fraction, which by definition ranges from 0 to 1.0, depending on phase incoherencies, can be roughly estimated from the data acquired for relative $B_{1,k}^{+}$ phase mapping. Indeed, the signal intensity of the low flip angle GRE images is approximately proportional to the flip angle, the latter being in turn proportional to B_1^+ magnitude. As a result, forming the ratio between MOS and SOM with the low flip angle GRE images acquired while transmitting with a single coil at a time provides an approximation of B_1^+ transmit efficiency. The sum of magnitudes (SOM) can be written as:

$$\mathrm{SOM}=\sum_{j=1}^{N}\sum_{k=1}^{M}|\hat{\mathbf{p}}_{j,k}|. \quad [3]$$

and for any given set of phases α_k, the result that would occur when pulsing all coils simultaneously can be simulated numerically by applying those phases to the same data and computing the corresponding MOS:

$$\mathrm{MOS}=\sum_{j=1}^{N}\left|\sum_{k=1}^{M}(\hat{\mathbf{p}}_{j,k}\cdot e^{-i\alpha_k})\right|. \quad [4]$$

Thus, the ratio of MOS to SOM for a given α_k will predict the fraction of available B_1^+ over the slice when experimentally transmitting with all channels simultaneously. This ratio was calculated for an α_k identically equal to zero for all channels, in order to simulate the equal phase state, as well as with α_k set to the B_1^+ shim phases given by Eq. [2] in order to simulate the resulting image after B_1^+ shimming.

B_1^+ Magnitude Mapping

Mapping of the transmit B_1 magnitude was accomplished with a two flip angle approach (28). The sequence consisted of a GRE acquisition with the following parameters: FOV = 300 –320 mm, TR = 6 sec, TE = 4.1 ms, acquisition matrix = 128 × 128, and slice thickness of 5–10 mm. For final image reconstruction, images from each receive channel were simply combined as the root of the sum of squares. The two flip angle method relies on a higher flip angle being twice as large as the lower flip angle. Throughout the course of these studies the lower flip angle was increased (see Table 2) in an attempt to improve the quality of the measured B_1^+ maps, especially prior to B_1^+ shimming where the signal was noticeably weak in some places (note that varying the nominal flip angles does not affect the comparison of results between subjects).

Based on the two images acquired, the low flip angle is estimated by $\arccos(|S_2(r)/2S_1(r)|)$, where $S_2(r)$ and $S_1(r)$ are the signal intensities from the higher and lower flip angles, respectively. Background pixels were eliminated by signal intensity thresholding. Also, in our experiments the two flip angle method appeared to be effective only for low flip angles of at least ≈10°. Thus, B_1^+ magnitude cannot be reliably calculated in areas where the smaller flip angle is too low. To accommodate flip angles larger than 90°, the B_1^+ maps were unwrapped by mapping the signal ratio $|S_2(r)/2S_1(r)|$ to the correct part of the periodic function $|\cos(\Phi)|$, where Φ is the low flip angle. As unwrapping was only necessary after B_1^+ shimming, a starting point for the unwrapping was determined by using the product of the predicted relative transmit efficiency (RTE; described below) and the average flip angle determined prior to shimming.

B_1^+ mapping data were obtained simultaneously transmitting through all eight channels with different sets of $B_{1,k}^+$ transmit phases: equal phase across all channels (*equal phase*), azimuthally determined phases based on coil geometry (*geometric phase*) and phases determined by the local B_1^+ shim procedure (B_1^+ *shim phase*). In order to allow for direct comparison, B_1^+ mapping data for a given subject were acquired with the RF power determined when simultaneously transmitting with all channels with equal phase (except where otherwise specified).

Relative Transmit Efficiency (RTE)

The equivalent of the theoretical SOM was not physically measured in this study, thus eliminating the option of estimating the fraction of available B_1^+ from the measured B_1^+ magnitude maps. Therefore, the alternative was to report the RTE, which is defined as the postshim to preshim ratio of flip angles averaged over the prostate. The RTE generated from the B_1^+ mapping data, which were measured while transmitting RF over all channels simultaneously, will be referred to as the "measured" RTE. For comparison purposes, the "predicted" RTE, calculated from the data acquired while transmitting through a single channel, one at a time, is defined as the ratio between the MOS of the complex images with B_1^+ shim corrections, $\hat{\mathbf{p}}_{j,k} \cdot e^{-i\alpha k}$, to the MOS of the uncorrected complex images, $\hat{\mathbf{p}}_{j,k}$. The measured and predicted RTE were calculated with preshim flip angle values obtained with either equal or geometric phases, and thus will be designated as $\mathrm{RTE_e}$ and $\mathrm{RTE_g}$, respectively.

The RTE provides an estimation of the transmit efficiency achievable with the local B_1^+ phase shimming technique in comparison to an initial transmit phase (either equal or geometric). While it is possible by definition for RTE to be less than 1, this would require the B_1^+ shim phases to result in increased destructive interferences compared to the equal or geometric sets of phases within the ROI around the prostate. As this situation did not occur within the study, all reported RTE values are greater than 1.

SAR Modeling

Modeling was performed with the XFDTD software (Remcom, State College, PA) in order to simulate B_1^+ fields and SAR distributions. This software utilizes a finite difference time domain method to solve Maxwell's equations. We modeled an eight-element stripline coil

(coil 1), loaded by the male human model provided with the software. In order to reproduce the comparisons made with the experimental data, B_1^+ fields were produced when transmitting ne channel at a time. For each single transmitting channel the phase of the RF input was set to zero. The eight resulting complex B_1^+ maps were then combined following the methods described above for the experimental data. Briefly, an ROI was drawn around the prostate location and its average B_1^+ phase was determined for each transmitting coil. Three sets of B_1^+ phases were determined: equal phase, geometric phase, and B_1^+ shim phase. The ratios of MOS over SOM were then compared for those three different sets of B_1^+ phases.

Complex electric field maps (E) were also obtained for each individual transmit coil. For each phase set, the resulting complex E fields (E_x, E_y, and E_z) were obtained by summing the electric field maps after applying the corresponding RF phases. SAR was calculated according to the standard formula:

$$SAR \propto \frac{\sigma}{\rho}(|\vec{E}_x|^2+|\vec{E}_y|^2+|\vec{E}_z|^2), \quad [5]$$

where ρ is the proton density and σ the conductivity of the tissues. In order to simulate the impact of B_1 shimming on SAR distributions, SAR maps were produced for the three B_1^+ phase sets with an identical, arbitrary RF input power for each coil element. Then the same SAR maps were compared after rescaling in order to obtain an equal B_1^+ magnitude in the prostate ROI (corresponding to an equal flip angle). We calculated the ratio of the average B_1^+ magnitude of the equal phase set (taken as a reference) to the average B_1^+ magnitude of the geometric and of the B_1 shim phase sets. The square of those ratios were used to rescale the SAR maps.

RESULTS

Relative Transmit Phase and Magnitude

Magnitude images and relative transmit phase images are shown for each transmit channel (Fig. 2). The magnitude images (Fig. 2a) were calculated by summing the magnitude of all receive channels after transmitting from a single channel,

$$\mathbf{A}_k=\sum_{j=1}^{N}|\hat{\mathbf{p}}_{j,k}|.$$

The position of the element, k, through which RF was transmitted to acquire each image is graphically depicted with a horizontal bar and labeled with its element number. In the magnitude images, some areas of relatively high signal are located in the vicinity of coils other than the one utilized for RF transmission (Fig. 2a), suggesting some residual coupling between different coils. Note that the magnitude images do not represent the absolute B_1^+ profiles as the signal intensity is also determined (among other factors) by proton density and receive B_1 (B_1^-) profiles. Only the relative transmit phases Ψ_k shown in Fig. 2b, as

calculated by Eq. [1], are needed for the B_1^+ shim technique presented here. As channel one is arbitrarily chosen as the phase reference, its relative transmit phase map is uniformly zero.

Local B_1^+ Shimming

A typical ROI defined for local B_1^+ shimming is shown on an SOM image in Fig. 3a (here for Subject 1). The B_1^+ shim phases determined with the B_1^+ shimming algorithm for all coil-subject combinations are shown in Table 1 (the phase of channel 1, taken as a reference, is always set to zero by definition). The B_1^+ shim phases presented in Table 1 are the conjugate values of α_k determined in Eq. [2]. As all single channel transmit data were obtained with an equal RF input phase, B_1^+ shim phases can be directly compared with the geometric phases based on coil geometry, also shown in Table 1. The standard geometric phases were determined for each of the two coil configurations, assuming that the prostate was positioned at the center of the body, with a distance between the anterior and posterior plates of 20 cm. It can be seen that the B_1^+ shim phases for a given coil configuration greatly vary from the phases dictated by coil geometry. As differences in anatomy between patients are expected to impact the actual B_1^+ shim phases, in-plane body measurements obtained in the transverse images utilized for B_1^+ shimming are also reported for each volunteer in Table 1 (29).

The complete B_1^+ shim procedure could be executed in less than 3 min with digitally controlled RF phase shifters. However, with the current hardware setup, the total time, including RF cable manipulations, was ≈15–20 min per subject.

Predicted Transmit Efficiency

By using the data obtained with one coil transmitting at a time it is theoretically possible to predict the increase in the fraction of available B_1^+ and the RTE that would be obtained with all coils transmitting simultaneously for any given set of B_1^+ phases (30). For any pixel, the best solution in terms of B_1^+ efficiency is to eliminate all B_1^+ cancellation between the eight transmit channels. Thus, the SOM image, defined in Eq. [3] and shown in Fig. 3a, is a synthesized map showing for each pixel the maximum image intensity that would be obtained in the absence of transmit B_1 cancellation (assuming that all data are obtained within a small flip angle regime). This SOM image exhibits nonuniformities resulting from proton density distribution as well as from magnitude profiles of both transmit and receive B_1 fields. Although it would be impossible to experimentally achieve such an absence of B_1^+ cancellation over the entire field of view, it is possible to approach, with B_1^+ shimming, this ideal situation within a focal region. The images shown in Fig. 3b, c represents two different MOS reconstructions of the same data, utilizing either the set of equal phases (Fig. 3b) or the set of B_1^+ shim phases α_k (Fig. 3c). Only B_1^+ cancellation varies between the three calculated images, whereas proton density and magnitude receive B_1^+ profiles are identical. As a result, and since all calculated images in Fig. 3 are shown with the same dynamic range, signal intensities can be compared to qualitatively assess the degree of signal loss due to B_1^+ cancellation in Fig. 3b, c relative to a complete absence of cancellation as shown in Fig. 3a.

A way to visualize the fraction of available B_1^+ before and after B_1^+ shimming is to generate images showing the ratio of MOS to SOM (proton density and receive B_1 profile components disappear when forming this ratio). Figure 4a, b shows such B_1^+ efficiency maps without and with B_1^+ shim phases, respectively. The ratio of the two maps (with to without B_1^+ shim phases) averaged over the region of the prostate provides what was defined in Materials and Methods as the predicted relative transmit efficiency (predicted RTE). The predicted RTE values are shown in Table 2 for all eight subjects. In our experiments the initial phase scheme utilized before B_1^+ shimming was always the equal phase condition resulting in RTE_e values, except for Subject 7, where the geometric phase scheme was used resulting in the calculation of RTE_g. Figure 4 illustrates typical results obtained with Subject 1. Prior to B_1^+ shimming ≈32% of the available B_1^+ is realized in the region of the prostate when transmitting with all coils (Fig. 4a). After B_1^+ shimming, ≈87% of the available B_1^+ is realized within the same ROI (Fig. 4), corresponding to a predicted RTE_e of 2.72. The average predicted RTE across all subjects was 4.5 ± 2.2 (Table 2). Note that these predicted RTE results are numerically derived from the B_1^+ shimming data specifically acquired when transmitting one channel at a time, whereas all other acquisitions, including prostate imaging and magnitude B_1^+ mapping, were obtained with all transmit coils pulsing the RF simultaneously.

B_1^+ Magnitude Maps

The proposed B_1^+ shimming methods were validated by generating B_1^+ maps both before and after the implementation of B_1^+ shim phases, allowing the evaluation of the measured RTE and B_1^+ nonuniformity within an ROI around the prostate. Representative B_1^+ maps obtained with equal B_1^+ phases and with B_1^+ shim phases are shown in Fig. 4c, d, respectively. These data were acquired while transmitting with all channels simultaneously as opposed to the fractional B_1^+ availability maps given in Fig. 4a, b. In this example the B_1^+ maps prior to shimming demonstrate large B_1^+ inhomogeneities within the prostate area, resulting in a complete loss of signal moving toward the rectum (Fig. 4c). After implementation of the B_1^+ shim phases, the measured B_1^+ map shows significant increase in flip angle as well as much higher uniformity in the region of the prostate (Fig. 4d). The average flip angles and standard deviations over the prostate obtained prior to and after B_1^+ shimming are shown for each subject in Table 2 along with the percent B_1^+ nonuniformity and measured RTE. The B_1^+ nonuniformity, defined as the flip angle standard deviation over the mean in the region of the prostate, is reported for each subject with average values across all eight subjects of 37 ± 8%, 24 ± 9%, and 5 ± 4% for the equal, geometric, and B_1^+ shim phase sets, respectively. The measured relative transmit efficiencies averaged across all patients were 4.2 ± 2.7 for RTE_e and 5.2 ± 2.4 for RTE_g (Table 2)

The regions used to calculate the values presented in Table 2 from the B_1^+ maps were determined by locations within the prostate that provided reliable flip angle measurements during the equal or geometric transmit phase conditions. While the nominal B_1^+ mapping flip angles were always reached at some location near to the prostate, the average flip angles were always much lower (Table 2).

SAR Modeling

Finite-difference time domain modeling of coil one with Remcom's body model are shown for a single slice through the male pelvis at the level of the prostate (Fig. 5). In Fig. 5 the three rows correspond to the ratio of MOS to SOM (available B_1^+), SAR with respect to an equal mean RF input power, and SAR with respect to an equal mean B_1^+ magnitude in the prostate (top to bottom). Within each row the images represent the equal, geometric, and B_1^+ shim sets of transmit phases (left to right). The modeled MOS to SOM ratios for the equal phases (Fig. 5a) and B_1^+ shim phases (Fig. 5c) are very similar to those obtained with the experimental B_1^+ shim calibration data for the same transmit phases, Fig. 4a, b, respectively. This similarity can be best appreciated by the "S" shape pattern of increased available B_1^+ in both Figs. 4b and 5c. This similarity between the modeled and the measured MOS to SOM ratios gives us confidence that the modeled SAR maps (a quantity we cannot experimentally measure) are reasonable. For a given input RF power (Fig. 5, row 2), the geometric phase set increases the relative peak SAR values at some locations in the pelvis (Fig. 5e) while the available B_1^+ is not improved in the prostate (Fig. 5b). For the B_1^+ shim phases the relative peak SAR at some locations in the pelvis are increased even further (Fig. 5f), but this time accompanied by a tremendous increase in the available B_1^+ in the region of the prostate (Fig. 5c).

The SAR maps rescaled to maintain an equal mean B_1^+ magnitude in the region of the prostate are shown in Fig. 5, row 3. The B_1^+ magnitude ratios were calculated for the geometric and B_1^+ shim phases (1.13 and 0.47, respectively), and the square of those ratios (1.23 and 0.22, respectively) were used to rescale the SAR maps. Note that the inverse of the B_1^+ magnitude ratio between equal versus B_1^+ shim phase sets (1/0.47 = 2.1), which is the simulated RTE_e, is on the low end of the measured RTE_e averaged over seven volunteers, 4.2 ± 2.7. Therefore, the model provides a conservative estimate of the potential benefits of local B_1^+ phase shimming on local SAR.

The geometric phase data demonstrates poor performance in comparison to the equal phase data in terms of available B_1^+ (Fig. 5b) and local SAR maxima (Fig. 5h). In the case of the B_1^+ shim phases, the large RF power reduction (by a factor $(0.22^{-1} = 4.55)$ resulting from the increased transmit efficiency (Fig. 5c) more than compensates for the local relative SAR maxima that may occur in some locations (Fig. 5i). As a result, for an equal mean flip angle in the prostate region, both local and global SAR were significantly reduced after B_1^+ shimming compared with the equal and geometric transmit phase sets.

Prostate Imaging

Both GRE and TSE anatomic imaging were performed, while simultaneously transmitting through all eight channels, at the same transverse slice position as the B_1^+ shimming calibration scan and mapping. The entire FOV is shown in Fig. 6, which demonstrates the large signal heterogeneity over the entire pelvis both before and after B_1^+ shimming. However, the signal voids seen within the prostate before B_1^+ shimming are removed when optimized transmit phases are used, both for GRE and TSE acquisitions, as shown in Fig. 6b, d. As expected, the signal intensity of the GRE acquisition is more tolerant of flip angle

inhomogeneities as it is proportional to the $|\sin(\gamma \tau B_1^+)|$ while the TSE acquisition is proportional to $|\sin^3(\gamma \tau B_1^+)|$.

The anatomic details and signal homogeneity made possible by B_1^+ shimming are shown in Fig. 7, which demonstrates the clear delineation of anatomical features in the prostate and surrounding structures. Figure 7a, b shows transverse GE and TSE acquisitions, respectively, from the same location of Subject 2, a 25-year-old male. The small transition zone expected in younger males (Fig. 7b) can be compared with the transition zone from Subject 6, a 55-year-old man (Fig. 7c).

While the B_1^+ shimming in this study was performed over a region selected from a 1-cm thick transverse slice, the results are adequate to obtain high-quality T_2w TSE images over the entire gland. This is shown in Fig. 8, which demonstrates excellent contrast and SNR homogeneity over the entire prostate with transverse, coronal, and sagittal slices from a 65-year-old man (Subject 5) after implementation of the B_1^+ shim phases. This result could be explained by the slower variations through space of B_1^+ coil profiles along the Z axis compared with the X and Y axes.

DISCUSSION

The results presented in this article demonstrate that despite difficulties encountered in the human body at magnetic fields as high as 7T, subject-dependent local B_1^+ shimming based solely on phase adjustments can be employed to greatly improve transmit efficiency and B_1^+ homogeneity over the human prostate. Images of the prostate after local phase B_1^+ shimming demonstrate the expected contrast as well as relatively uniform signal intensity over the extent of the gland. While the potential advantages of local transceiver coils for body applications have been shown previously at 3T (31,32) and 4T (18), our results demonstrate for the first time the successful application of a transmit/receive array placed in close proximity of the human body in conjunction with the calculation of subject-dependent B_1^+ shimming for successful torso imaging at 7T.

Usually, receive-only arrays placed in close proximity to the body are employed together with RF transmission through a large, circumscribing “body” coil that would generate a relatively homogeneous B_1^+ in the absence of the human body. We have previously shown that, as expected from high magnetic fields, RF inhomogeneities exist in the human torso at 7T (6) or even at 4T when using such a circumscribing “body” coil; we had also shown that B_1^+ shimming employed through adjustment of the phase and currents in the individual current carrying elements of the “body” coil can improve image homogeneity (33). However, these previous results were not based on subject-dependent adjustments which, as demonstrated here, are necessary for optimizing transmit efficiency as well as B_1^+ homogeneity.

The “drop out” of signal (Fig. 3b) and of B_1^+ (Fig. 6a, c) near the center of the body is a common problem at UHF, especially in body imaging as demonstrated in the work by Vaughan et al. (5). Transmit field inhomogeneity in body imaging has also been described as an issue on 3T clinical systems with whole body volume transmit and local parallel

receive coil configurations, and even at 1.5T the same phenomenon occurs, as initially described in the human torso by Glover et al. (34). However, at 3T and lower fields this problem has only a limited impact, so that it remains feasible to acquire and interpret body images utilizing a traditional large body RF coil (35,36). At UHF the RF wavelength in the body decreases further, from ≈30 cm at 3T to 12 cm at 7T. In this situation, B_1^+ destructive interferences due to incoherent phase distributions, a mechanism fully demonstrated in the head at 7T (12), are much more pronounced, even in coil configurations that generate uniform B_1^+ fields in the absence of a load. Additionally, the magnitude of each individual coils B_1^+ profile exhibits larger distortion through space, both effects leading to large B_1^+ field inhomogeneity and subsequent signal and contrast variations. Local B_1^+ phase shimming on the prostate greatly reduces local B_1^+ losses, due to a reduction of destructive interferences. As a result, the total B_1^+ magnitude obtained in the prostate with the set of B_1^+ shim phases when all coils are transmitting together is very close to the sum of the eight individual $B_{1,k}^+$ magnitudes in the same location. Correspondingly, computing the MOS image as in Fig. 3c, with the same set of B_1^+ shim phases, produces a prediction image close to an ideal SOM reconstruction in the region of the prostate (Fig. 3a). A striking observation is that, besides the tangible gains obtained within the prostate, little to no benefit is realized for the rest of the pelvis.

Local B_1^+ Shimming Performance

The primary benefit of local B_1^+ shimming through transmit phase optimization is an increase in transmit efficiency; however, a tremendous increase in B_1^+ homogeneity was also observed in this study in comparison to both the equal and geometric transmit phase configurations. Such improvements in homogeneity are likely a result of the fortuitous position of the prostate, which is typically close to the center of the transmit coil array and of the torso. It seems probable that for other ROIs located within the close vicinity of a transmit element (37) the same improvement in B_1^+ homogeneity may not be achieved with B_1^+ shimming solely based on relative B_1^+ phase mapping. In such cases the B_1^+ magnitude profiles of each individual transmit element may also have to be considered in order to increase B_1^+ homogeneity (note that optimizing on B_1^+ homogeneity would in turn involve some degree of local B_1^+ magnitude losses). A fundamental observation in the present study is that, despite an approximately symmetric system formed by an array coil and a volunteer's torso, large variations in needed B_1^+ phase corrections over the prostate were observed between subjects, thus demonstrating the importance of mapping B_1^+ phases in each subject in order to perform successful, subject-dependent B_1^+ shimming at UHF.

The local B_1^+ shimming algorithm presented here was designed to optimize B_1^+ within relatively small regions of interest. As the ROI increases in size, the method of averaging phases across that region to determine α_k may fail because of a lack of phase coherence within the B_1^+ profile of a single transmit element over a larger spatial scale. B_1^+ shimming over larger volumes requires additional B_1^+ magnitude information.

A significant advantage of the local B_1^+ phase shimming technique presented here is its limited hardware requirements. Indeed, with only one RF amplifier and with a standard single transmit channel, it was possible to achieve spectacular improvements when imaging

the prostate. In general, MR scanners could be retrofitted to offer such capability with transmit coil arrays, one of the main constraints being most likely the installation of multiple T/R switches when both transmit and receive utilization of each coil element is desired. If separate receive coils were utilized this constraint would vanish, although efficient coil decoupling would naturally be required between transmit and receive-only coil elements. In order to achieve even higher levels of B_1^+ optimization, it would be necessary to modulate the individual RF input amplitudes as well, requiring more demanding hardware configurations (17,20).

Transmit Efficiency and SAR

The ability to reduce transmitter power through the more efficient use of RF has significant ramifications for imaging studies at UHF. One of the major hurdles facing UHF imaging is that of absorbed RF power reported as the specific absorption rate (SAR). FDA guidelines limiting SAR do not increase with the static field strength (B_0) while the amount of RF actually absorbed increases proportional to B_02. Therefore, at a higher B_0, more power is required to achieve a desired B_1^+, resulting in increased SAR even in the absence of destructive interferences. In the presence of destructive interferences this problem of increased required power and SAR is further exacerbated. By using the applied B_1^+ more efficiently through B_1^+ shimming, the corresponding electric fields (E-fields), which are responsible for heating, are on average scaled proportionately. More important, our SAR modeling results indicate that the increase in transmit efficiency in the optimized region greatly reduces the required input power (Fig. 5). This reduction more than compensated for any increase in local SAR maxima resulting from local B_1^+ shimming, at least in the transverse section shown. Experimentally, as averaged over the eight subjects in this study, the increased transmit efficiency resulted in a transmit voltage decrease from 699 V pre- to 197 V post-B_1^+ shim for a 500 μs square RF pulse to achieve a 90° flip angle in the prostate.

The current modeling results are based on comparing SAR values calculated by normalizing the B_1^+ magnitude of the geometric and B_1^+ shim phase data to that of the equal phase data. Although the patterns of available B_1^+ were noticeably similar in modeling and experimental data, it should be noted that the modeling results were based on a body model of a fixed size that was not equivalent to the body size of the subject in Fig. 4. More accurate and quantitative results will require matching the body model to the size of the subjects studied and carefully calibrating the input power used for modeling. While the electrodynamic modeling incorporated the entire body model, the present SAR results were obtained from a single axial slice at the level of the prostate; future developments will include larger 3D analysis of SAR distributions throughout the body.

Simulated versus Measured Transmit B_1^+

Predicted and measured RTE values were within 6% of each other in phantom studies (data not shown) and within 10% across seven subjects, as shown in Table 2 (predicted RTE of 4.5 ± 2.2 and measured RTE of 4.2 ± 2.7). However, for each individual there was a significant difference between the measured and predicted RTE values which can result from a combination of several factors: variable T_1 saturation when measuring the B_1^+ maps, variable T_1 weighting in the measurements used for B_1^+ shimming, low SNR and poor

stability of B_1^+ maps at low flip angles especially in the equal and geometric phase conditions, poor performance of the two flip angle methods with flip angles near multiples of 90°, variable performance of slice selective RF pulses with widely varying flip angles (38), coil-to-coil coupling variations between single channel and simultaneous transmit modes and motion during and between the acquisition of each dataset used to calculated the B_1^+ maps. The primary factors contributing to individual discrepancies will have to be studied further, as they were not specifically investigated in this work. While it would be helpful for optimization routines to accurately predict potential local B_1^+ gains, this is not necessary for performing the presented methods because relative phase calculations are independent of the corresponding magnitudes (except for the possibility of excessive noise in the low flip angle calibration images).

Future comparisons of B_1^+ shimming methods with preshimmed results will benefit from performing individual power calibrations prior to measuring the B_1^+ maps, thereby minimizing the range of values that need to be accommodated. As observed in this study, the potential increase in transmit efficiency can quickly result in an over 7-fold increases in local B_1^+ with shimming.

Coil Geometry

Li et al. (39) simulated B_1^+ shimming, also referred to as field focusing, using both phase and amplitude modulations for cardiac imaging using an eight-element transceiver phased array coil to improve B_1^+ homogeneity across the heart. While this simulation study predicted the benefit of B_1^+ shimming in the body at 2T, in practice the unique body geometry and coil placement obtained for a given individual would likely require a patient-dependent solution, especially at UHF, as demonstrated by our results in the prostate at 7T. The requirement of direct RF inhomogeneity measurements for a given subject in order to implement B_1^+ shimming has also been mentioned by Ulloa et al. (40). In addition, it has been reported with head coils that the coil diameter, the number of coil elements, as well as the geometry of the head itself can significantly impact B_1^+ profiles (37,41). The issues raised in these previous reports are exacerbated in the present UHF body imaging study because of the flexible transceive array coil closely coupled to the body and the widely varying geometries of the human torso and pelvis. These results highlight the importance of subject-specific B_1^+ calibrations instead of solutions solely based on coil design. While phases determined by coil geometry performed slightly better than equal phases across all transmit channels, the phases determined by B_1^+ shimming were far superior (Table 2). Potentially, average values obtained for both coil geometries could be used as starting point for B_1^+ optimization, and additional parameters such as body geometry measured in scout images could be utilized to refine such average numbers. Starting with those values, closer to an optimum, would likely improve initial calibration and B_1^+ mapping prior to implementing B_1^+ shim corrections.

Recently, prostate imaging at 4T by Pinkerton et al. (18) has been shown to benefit from transmit phase driving schemes other than conventional circularly polarized. However, they acknowledge the limitation of the fixed hardware solution presented, as the optimal driving schemes will ultimately depend on body geometry, and their approach did not utilize actual

B_1^+ measurements. With the eight healthy subjects imaged in this study, geometry differences were observed when comparing both the dimensions in the transverse plane and the relative anterior to posterior position of the prostate. In general, these variations would be even larger in the general patient population, requiring a subject dependent B_1^+ shimming approach, such as proposed in this work, for optimal transmit efficiency and homogeneity.

Comment on SNR

Theoretical calculations as well as numerous experimental studies conducted on the human head have demonstrated that SNR increases about linearly with field strength in frequencies ranging from 64 to 300 MHz (2,27,42–44). These gains are expected to be realized in the human body as well and, in fact, have been demonstrated in cardiac studies conducted at 4T (45). Similar field strength-dependent gains in SNR are expected in human prostate at 7T provided destructive interferences are eliminated and optimal signal excitation is achieved, as it was with the B_1 shimming methods presented here. In fact, the T_2w images shown, when compared to those obtained with an eight-channel surface coil at 3T, suggests that indeed the gains are at least, if not better than, the expected SNR increase of 7/3. However, this must remain as a qualitative assessment at this stage because SNR comparisons are difficult to achieve experimentally and require extreme attention to detail. To adequately address this issue of SNR a careful study would have to be performed addressing the many hardware differences, including the complete transceiver pathway as well as coil geometry and performance. This was not the aim of this work. Rather, we aimed to show that potential hurdles to realize the maximal SNR at UHF can be overcome.

CONCLUSIONS

Significantly increased transmit efficiency and B_1^+ homogeneity can be achieved in the prostate at 7T by minimizing destructive B_1^+ interferences with an eight-channel stripline array through local B_1^+ phase shimming. This optimization is performed by adjusting transmit phases determined from subject-dependent calibration measurements. While tremendous B_1^+ inhomogeneities exist in body imaging at UHF, the relatively small volume of the prostate enables this straightforward phase-based optimization to achieve excellent results with only limited hardware and calibration requirements. Modeling results indicate large SAR reduction after B_1^+ shimming due to the significantly decreased RF power needed for a given flip angle in the prostate region. The minimization of destructive B_1^+ interferences through subject-dependent local phase B_1^+ shimming resulted in the acquisition of high-quality GRE and TSE prostate images at 7T.

Acknowledgments

The authors thank Gregor Adriany for useful discussions.

Grant sponsor: National Institutes of Health (NIH); Grant numbers: P41 RR08079, R01 EB000895-04, S10 RR1395; Grant sponsor: Keck Foundation; Grant sponsor: National Science Foundation (NSF); Grant number: 9907842.

References

1. Rouviere O, Hartman RP, Lyonnet D. Prostate MR imaging at high-field strength: evolution or revolution? Eur Radiol. 2006; 16:276–284. [PubMed: 16155721]
2. Vaughan JT, Garwood M, Collins CM, Liu W, DelaBarre L, Adriany G, Andersen P, Merkle H, Goebel R, Smith MB, Ugurbil K. 7T vs. 4T: RF power, homogeneity, and signal-to-noise comparison in head images. Magn Reson Med. 2001; 46:24–30. [PubMed: 11443707]
3. Tkac I, Andersen P, Adriany G, Merkle H, Ugurbil K, Gruetter R. In vivo 1H NMR spectroscopy of the human brain at 7 T. Magn Reson Med. 2001; 46:451–456. [PubMed: 11550235]
4. Wiesinger F, Van de Moortele PF, Adriany G, De Zanche N, Ugurbil K, Pruessmann KP. Parallel imaging performance as a function of field strength—an experimental investigation using electrodynamic scaling. Magn Reson Med. 2004; 52:953–964. [PubMed: 15508167]
5. Vaughan JT, DelaBarre L, Snyder C, Tian J, Bolan P, Garwood M, Adriany G, Strupp JP, Andersen P, Van de Moortele PF, Ugurbil K. Highest field human MR imaging. IEEE Trans EMC. 2006:213.
6. Vaughan, JT.; Snyder, C.; DelaBarre, L.; Bolinger, L.; Tian, J.; Andersen, P.; Strupp, JP.; Adriany, G.; Ugurbil, K. 7T body imaging: first results. Proc 14th Annual Meeting ISMRM; Seattle, WA. 2006; p. 213
7. Vaughan, JT. High frequency coils. In: Robitaille, PL.; Berliner, LJ., editors. Ultra high field magnetic resonance imaging and spectroscopy. Vol. 26. New York: Springer; 2006. p. 127-161.
8. Bottomley PA, Andrew ER. RF magnetic field penetration, phase shift and power dissipation in biological tissue: implications for NMR imaging. Phys Med Biol. 1978; 23:630–643. [PubMed: 704667]
9. Glover GH, Hayes CE, Pelc NJ, Edelstein WA, Mueller OM, Hart HR, Hardy CJ, Odonnell M, Barber WD. Comparison of linear and circular-polarization for magnetic-resonance imaging. J Magn Reson. 1985; 64:255–270.
10. Yang QX, Wang J, Zhang X, Collins CM, Smith MB, Liu H, Zhu XH, Vaughan JT, Ugurbil K, Chen W. Analysis of wave behavior in lossy dielectric samples at high field. Magn Reson Med. 2002; 47:982–989. [PubMed: 11979578]
11. Kangarlu A, Baertlein BA, Lee R, Ibrahim T, Yang L, Abduljalil AM, Robitaille PM. Dielectric resonance phenomena in ultra high field MRI. J Comput Assist Tomogr. 1999; 23:821–831. [PubMed: 10589554]
12. Van de Moortele PF, Akgun C, Adriany G, Moeller S, Ritter J, Collins CM, Smith MB, Vaughan JT, Ugurbil K. B(1) destructive interferences and spatial phase patterns at 7 T with a head transceiver array coil. Magn Reson Med. 2005; 54:1503–1518. [PubMed: 16270333]
13. Collins CM, Liu W, Schreiber W, Yang QX, Smith MB. Central brightening due to constructive interference with, without, and despite dielectric resonance. J Magn Reson Imaging. 2005; 21:192–196. [PubMed: 15666397]
14. Hoult D. The principle of reciprocity in signal strength calculations —a mathematical guide. Concepts Magn Reson. 2000; 12:173–187.
15. Vaughan JT, Hetherington HP, Otu JO, Pan JW, Pohost GM. High frequency volume coils for clinical NMR imaging and spectroscopy. Magn Reson Med. 1994; 32:206–218. [PubMed: 7968443]
16. Boskamp, E.; Lee, R. Whole body LPSA transceive array with optimized transmit homogeneity. Proc 10th Annual Meeting ISMRM; Honolulu, HI. 2002; p. 903
17. Katscher U, Bornert P, Leussler C, van den Brink JS. Transmit SENSE. Magn Reson Med. 2003; 49:144–150. [PubMed: 12509830]
18. Pinkerton RG, Near JP, Barberi EA, Menon RS, Bartha R. Transceive surface coil array for MRI of the human prostate at 4T. Magn Reson Med. 2007; 57:455–458. [PubMed: 17260367]
19. Adriany G, Van de Moortele PF, Wiesinger F, Moeller S, Strupp JP, Andersen P, Snyder C, Zhang X, Chen W, Pruessmann KP, Boesiger P, Vaughan T, Ugurbil K. Transmit and receive transmission line arrays for 7 Tesla parallel imaging. Magn Reson Med. 2005; 53:434–445. [PubMed: 15678527]

20. Vaughan T, Delabarre L, Snyder C, Tian J, Akgun C, Shrivastava D, Liu W, Olson C, Adriany G, Strupp J, Andersen P, Gopinath A, van de Moortele PF, Garwood M, Ugurbil K. 9. 4T human MRI: preliminary results. Magn Reson Med. 2006; 56:1274–1282. [PubMed: 17075852]
21. Van de Moortele, PF.; Snyder, C.; DelaBarre, L.; Akgun, C.; Wu, X.; Vaughan, JT.; Ugurbil, K. Fast mapping of relative B1+ phase in the human head at 9.4 Tesla with a 14 channel transceive coil array. Int Symp Biomed Magn Reson Imaging Spectrosc Very High Fields; Wurzburg, Germany. 2006;
22. Yang QX, Mao W, Wang J, Smith MB, Lei H, Zhang X, Ugurbil K, Chen W. Manipulation of image intensity distribution at 7. 0 T: passive RF shimming and focusing with dielectric materials. J Magn Reson Imaging. 2006; 24:197–202. [PubMed: 16755543]
23. Metzger, G.; Van de Moortele, PF.; Snyder, C.; Vaughan, JT.; Ugurbil, K. Local B1 shimming for imaging the prostate at 7 Tesla. Proc 15th Annual Meeting ISMRM; Berlin, Germany. 2007; p. 799
24. DelaBarre, L.; Snyder, C.; Van de Moortele, PF.; Akgun, C.; Ugurbil, K.; Vaughan, JT. Cardiac imaging at 7T. Proc 15th Annual Meeting ISMRM; Berlin, Germany. 2007; p. 3867
25. Snyder, CJ.; DelaBarre, L.; Van de Moortele, PF.; Snyder, A.; Akgun, C.; Jinfeng, T.; Metzger, G.; Ugurbil, K.; Vaughan, JT. Stripline/TEM transceiver array for 7T body imaging. Proc 15th Annual Meeting ISMRM; Berlin, Germany. 2007; p. 164
26. Wang, J. A novel method to reduce the signal coupling of surface coils for MRI. Proceedings of the 4th Annual Meetings of ISMRM; New York. 1996; p. 1434
27. Collins CM, Smith MB. Signal-to-noise ratio and absorbed power as functions of main magnetic field strength, and definition of “90 degrees” RF pulse for the head in the birdcage coil. Magn Reson Med. 2001; 45:684–691. [PubMed: 11283997]
28. Insko E, Bolinger L. Mapping of the radiofrequency field. J Magn Reson Ser A. 1993; 103:82–85.
29. Van den Berg CA, van den Bergen B, Van de Kamer JB, Raaymakers BW, Kroeze H, Bartels LW, Lagendijk JJ. Simultaneous B1 + homogenization and specific absorption rate hotspot suppression using a magnetic resonance phased array transmit coil. Magn Reson Med. 2007; 57:577–586. [PubMed: 17326185]
30. Van de Moortele, PF.; Snyder, C.; DelaBarre, L.; Adriany, G.; Vaughan, JT.; Ugurbil, K. Calibration tools for RF shim at very high field with multiple element RF coils: from ultra fast local relative phase to absolute magnitude B1+ mapping. Proc 15th Annual Meeting ISMRM; Berlin, Germany. 2007. p. 1676
31. Duensing, GR.; Peterson, DM.; Wolverton, BL.; Fitzsimmons, J. Transceive phased array designed for imaging at 3.0T. Proc 6th Annual Meeting ISMRM; Sydney, Australia. 1998; p. 441
32. Kim HW, Buckley DL, Peterson DM, Duensing GR, Caserta J, Fitzsimmons J, Blackband SJ. In vivo prostate magnetic resonance imaging and magnetic resonance spectroscopy at 3 Tesla using a transceive pelvic phased array coil: preliminary results. Invest Radiol. 2003; 38:443–451. [PubMed: 12821859]
33. Vaughan JT, Adriany G, Snyder CJ, Tian J, Thiel T, Bolinger L, Liu H, DelaBarre L, Ugurbil K. Efficient high-frequency body coil for high-field MRI. Magn Reson Med. 2004; 52:851–859. [PubMed: 15389967]
34. Glover GH, Hayes CE, Pelc NJ, Edelstein WA, Mueller OM, Hart HR, Hardy CJ, O’Donnel M, Barber WD. Comparison of linear and circular polarization for magnetic resonance imaging. J Magn Reson. 1985; 64:255–270.
35. von Falkenhausen MM, Lutterbey G, Morakkabati-Spitz N, Walter O, Gieseke J, Blomer R, Willinek WA, Schild HH, Kuhl CK. High-field-strength MR imaging of the liver at 3.0 T: intraindividual comparative study with MR imaging at 1. 5 T. Radiology. 2006; 241:156–166. [PubMed: 16908683]
36. Hussain SM, Wielopolski PA, Martin DR. Abdominal magnetic resonance imaging at 3.0 T: problem or a promise for the future? Top Magn Reson Imaging. 2005; 16:325–335. [PubMed: 16785848]
37. Van de Moortele, PF.; Akgun, C.; Snyder, C.; DelaBarre, L.; Adriany, G.; Vaughan, JT.; Ugurbil, K. Impact of coil diameter and number of coil elements on B1 destructive interferences with stripline coil arrays at 7 Tesla. Proc 14th Annual Meeting ISMRM; Seattle, WA. 2006; p. 3535

38. Hoult DI. Solution of the Bloch equations in the presence of a varying B1 field — approach to selective pulse analysis. J Magn Reson. 1979; 35:69–86.
39. Li BK, Liu F, Crozier S. Focused, eight-element transceive phased array coil for parallel magnetic resonance imaging of the chest—theoretical considerations. Magn Reson Med. 2005; 53:1251–1257. [PubMed: 15906277]
40. Ulloa, JL.; Irarrazaval, P.; Hajnal, JV. Exploring 3D RF shimming for slice selective imaging. Proceedings of the 13th Annual Meeting of ISMRM; Miami. 2005; p. 21
41. Collins CM, Swift BJ, Liu W, Vaughan JT, Ugurbil K, Smith MB. Optimal multiple-element ring configuration depends on head geometry, placement, and volume of interest. Proc Int Soc Magn Reson Med. 2004; 12:1566.
42. Hoult DI, Phil D. Sensitivity and power deposition in a high-field imaging experiment. J Magn Reson Imaging. 2000; 12:46–67. [PubMed: 10931564]
43. Keltner JR, Carlson JW, Roos MS, Wong STS, Wong TL, Budinger TF. Electromagnetic fields of surface coil in vivo NMR at high frequencies. Magn Reson Med. 1991; 22:467–480. [PubMed: 1812380]
44. Singerman RW, Denison TJ, Wen H, Balaban RS. Simulation of B1 field distribution and intrinsic signal-to-noise in cardiac MRI as a function of static magnetic field. J Magn Reson. 1997; 125:72–83. [PubMed: 9245362]
45. Wen H, Denison TJ, Singerman RW, Balaban RS. The intrinsic signal-to-noise ratio in human cardiac imaging at 1. 5, 3, and 4 T. J Magn Reson. 1997; 125:65–71. [PubMed: 9245361]

APPENDIX

Given the residual coupling between different coil elements, transmitting through a single channel actually results in transmitting not only through the coil element physically connected to this channel but also through all coupled coil elements. Formally, this can be written as:

$$\underbrace{\mathrm{B}_{1,k}^{+}}_{\text{Channel } k} = \sum_{t=1}^{M} \lambda_{k,t} \underbrace{\mathrm{B}_{1,t}^{+}}_{\text{Elements } t},$$

where λ is a complex coefficient, t is the index over coil elements, k is the index over transmit channels, and M, in this case, represents the total number of both transmit elements and channels. Practically, the RF shimming method proposed here depends on the ability to modify the phase of RF channels, not of individual coil elements. For this reason throughout the article we refer to the relative transmit phase, Ψ_k, for each channel k.

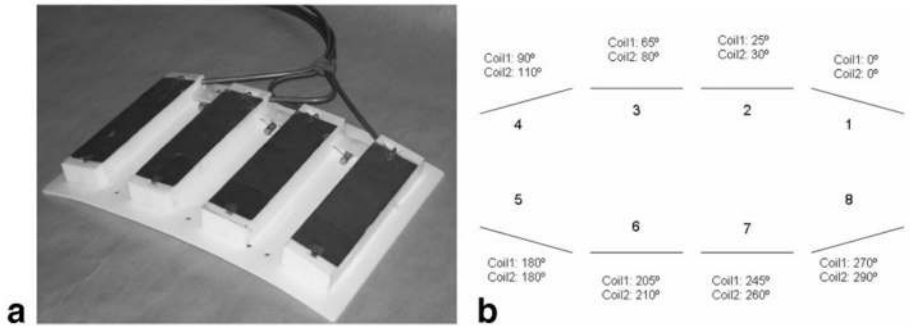

FIG. 1.

a: Anterior four elements of the eight-channel stripline torso array coil affixed to a flexible Teflon plate. As shown from the top, the 5.0 cm wide copper foil ground plates are visible. **b:** Schematic showing the relative element positions and numbering of the eight-channel torso array for both coils 1 and 2. For the two coils used in this study, transmit phases based on coil geometry were determined assuming a central region of interest and an anterior-posterior plate separation of 20 cm. The "geometric phase" for each element of the two-coil configurations are shown.

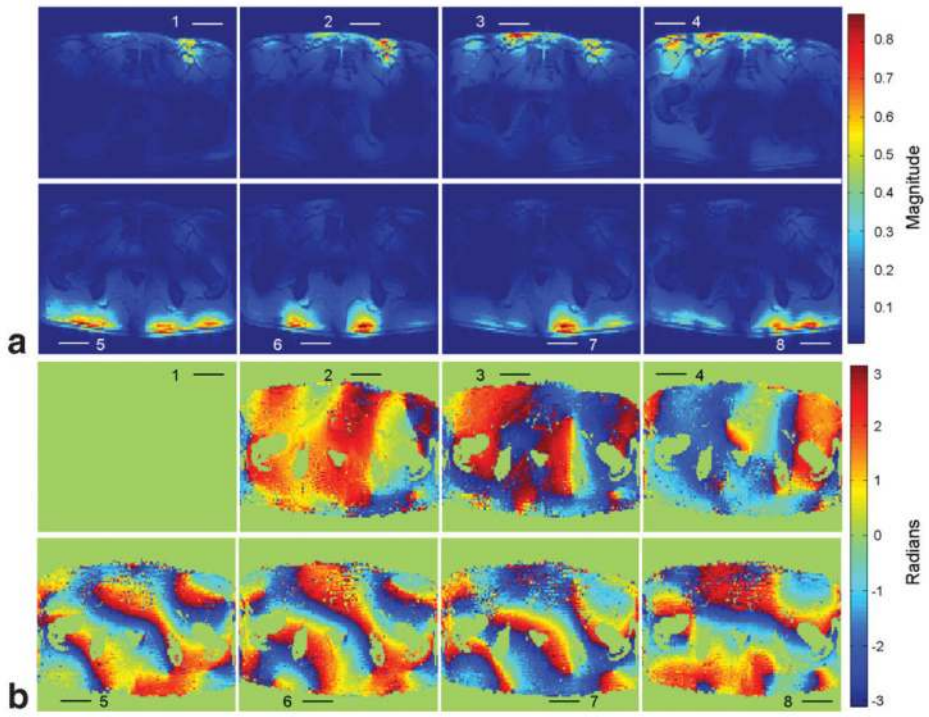

FIG. 2.

(**a**) Magnitude, $\mathbf{A}_k$, and (**b**) relative phase, Ψ_k, images acquired by transmitting through a single channel, k, and receiving on all channels. The magnitude images are created by the sum of magnitude images from each receive channel. The element positions are shown in each frame representing the location from which RF was transmitted. Various amounts of residual coupling are observed when transmitting through individual channels as suggested by increased signal at locations closer to other channels than the indicated transmitting element position. The relative transmit phase for element one shows zero phase throughout as this element is arbitrarily chosen as the reference channel as detailed in Eq. [1] of the B_1^+ shimming methods. Only the relative phases between transmit channels in (**b**) are important for the local B_1^+ shimming implemented in this study.

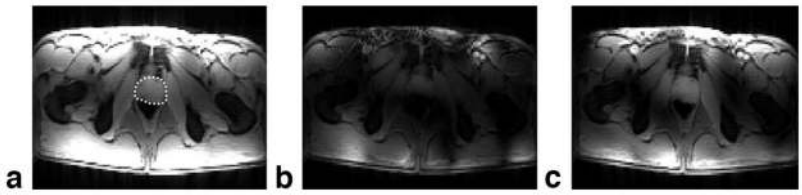

FIG. 3.

The subject-dependent data required to implement local B_1^+ shimming involved collecting a series of complex images by transmitting through each coil element, one at a time, while receiving on all channels. The sum of magnitude (SOM) of these complex images (**a**) is a synthesized image free from all destructive interferences between channels, and thus provides a reference by which all B_1^+ optimizations can be evaluated. The magnitude of the sum (MOS) provides the magnitude image after complex addition of the same data prior to (**b**) and after (**c**) the application of the calculated correction phases determined by local B_1^+ shimming. The signal intensities of all three images can be compared with respect to each other and used to qualitatively assess the increased efficiency and homogeneity of B_1^+ across the prostate.

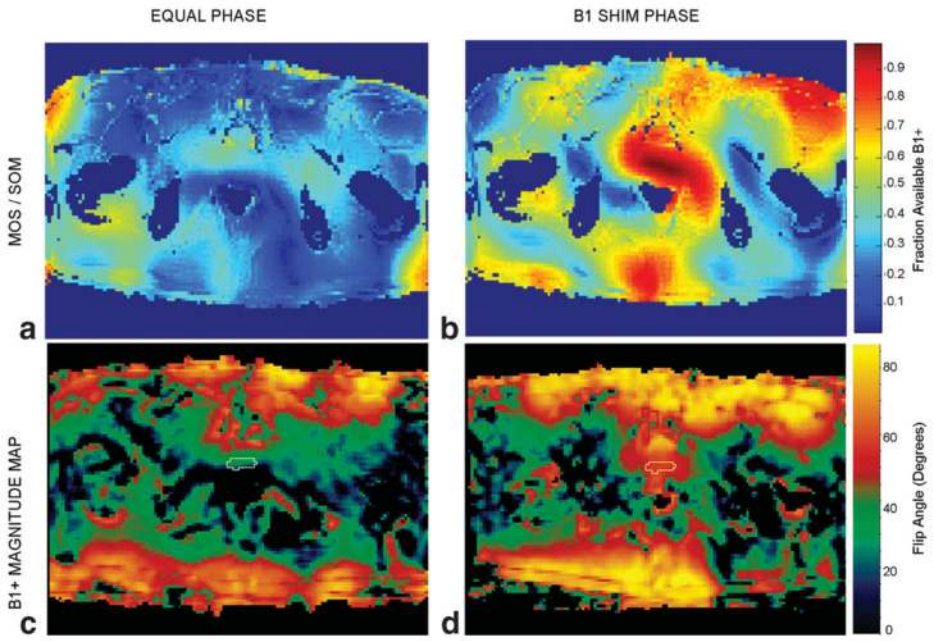

FIG. 4.

Images of both the theoretical fraction of available B_1^+ given by the MOS/SOM ratio with (**a**) equal phase and (**b**) B_1^+ shim phase along with the measured B_1^+ magnitude maps for (**c**) equal phase and (**d**) B_1^+ shim phase. For the MOS/SOM ratio images (**a, b**) the best case scenario is to have a value of 1.0 which would represent the most efficient use of the applied RF power. For the measured B_1^+ maps (**c, d**) the object is achieve the maximum flip angle possible given a constant transmit RF power. The MOS/SOM maps (**a, b**), which are generated from the data acquired while transmitting over each channel individually, qualitatively predict the outcome of simultaneously transmitting over all channels simultaneously, as is done for the B_1^+ maps (**c, d**), under each of the transmit phase schemes. In this case the fraction of available B_1^+ with equal phase (**a**) is only 0.32 while for the B_1^+ shim phase it is 0.87 (**b**) averaged over the prostate. The measured B_1^+ maps (**c, d**) show an increase in averaged flip angles from 23.6° and 53.5° between the equal and B_1^+ shim phase schemes. These values correspond to a predicted and measured RTE_e of 2.72 and 2.27, respectively.

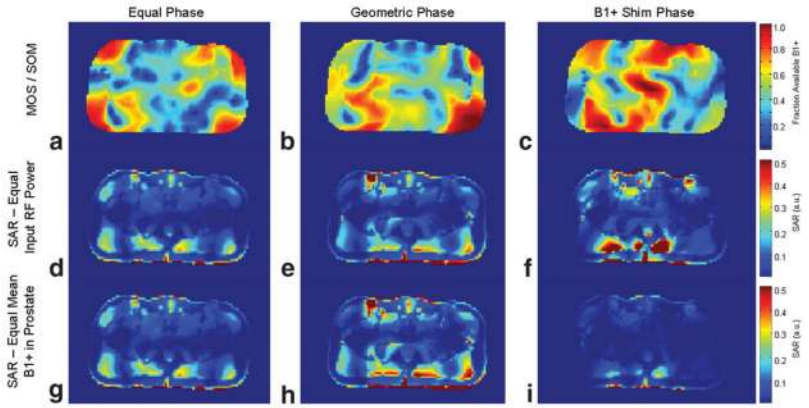

FIG. 5.

FDTD modeling data was used to calculate MOS to SOM ratios (top row), SAR with respect to an equal RF input power (middle row), and SAR with respect to an equal average B_1^+ magnitude in the prostate (bottom row). These results were constructed for the three sets of transmit phases used in this study: equal phase (left column), geometric phase (middle column), and B_1^+ shim phase (right column). The dynamic range of the SAR maps in the middle and bottom rows are identical to allow a direct comparison of values. While a maximum SAR value of 0.5 (in arbitrary units) was chosen to highlight the differences between the six maps, those values shown at the maximum typically extended well above 0.5 in some of the pictures, especially in (**f**). Because of the tremendous increase in transmit efficiency in the region of the prostate resulting from using B_1^+ shim phases (**c**), the power required to maintain an equal average B_1^+ in the prostate (relative to the equal phase state) dropped over 4-fold. Therefore, the increased local SAR maxima observed in (**f**), resulting from transmitting with the B_1^+ shim phases but with the same input RF power as in the equal phase state, are reduced below the level of those in (**g**) after accounting for the increased RF efficiency (**i**). For clarity, the same picture is shown in (**d**) and (**g**) because it represents the starting value in both rows.

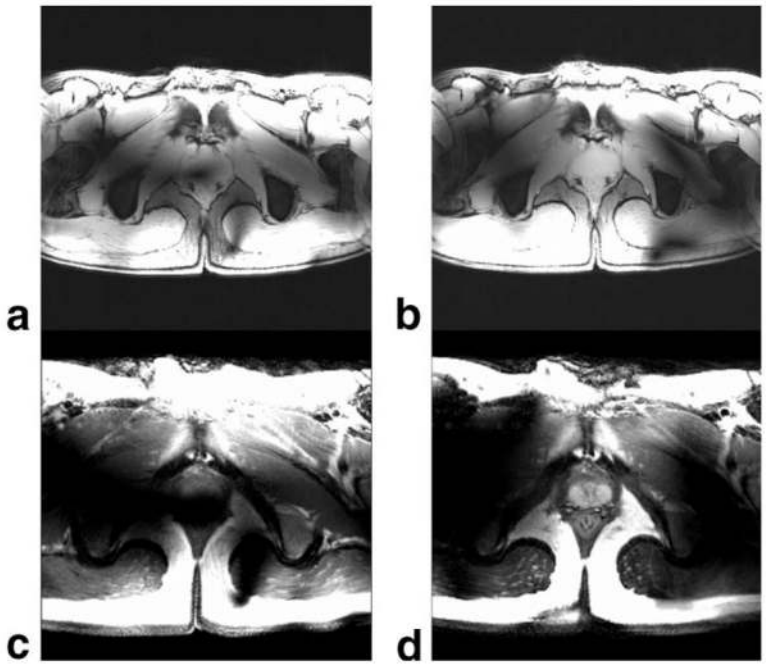

FIG. 6.

Anatomic images of the prostate (acquired transmitting with all channels simultaneously). Full FOV gradient echo (GE) images before (**a**) and after (**b**) B_1^+ shimming are shown. Full FOV Turbo-spin echo (TSE) images before (**c**) and after (**d**) B_1^+ shimming are shown. As expected, the TSE acquisition is more sensitive to the inhomogenous B_1^+ as demonstrated by the low SNR and absence of the expected contrast (**c**). For all subjects, successful TSE imaging was not possible until after the transmit phases were adjusted by focal B_1^+ shimming.

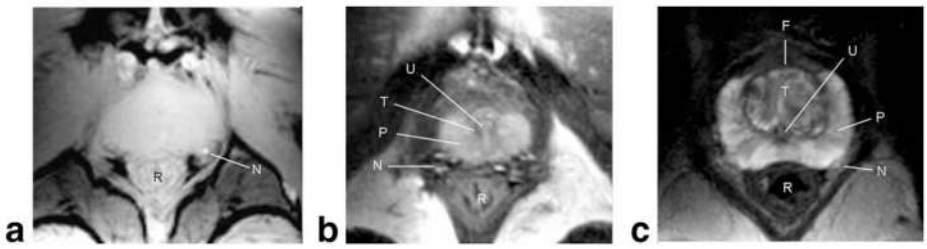

FIG. 7.

GE (**a**) and TSE (**b**) images of a 25-year-old male from the same transverse slice zoomed in to the region of the prostate after B_1^+ shimming. The arrows indicate various anatomical features of the prostate and surrounding structures: neurovascular bundle (N), rectum (R), urethra (U), transition zone (T), peripheral zone (P), and fibromuscular tissue (F). TSE image after B_1^+ shimming (**b**) provide the contrast necessary to appreciate the zonal anatomy of the prostate. An image from a similar transverse slice of a 55-year-old man (**c**) demonstrates the typical enlargement of the transition zone associated with aging.

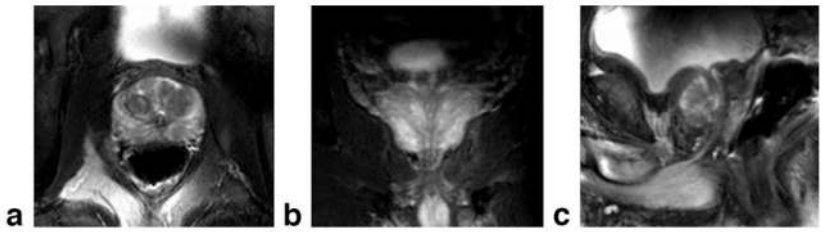

FIG. 8.

While B_1^+ shimming was performed over a region on a single 1-cm thick transverse slice, the field homogeneity was sufficient over a larger region, allowing high SNR and contrast T_2w TSE images to be acquired throughout the prostate. Axial (**a**), coronal (**b**), and sagittal (**c**) images from a 65-year-old man after B_1^+ shimming are shown with excellent anatomical detail.

Table 1

Left: Comparison of Transmit Phases Dictated by Coil Geometry and B_1^+ Shim Phases; the Latter Calculated from Subject-Dependent Calibration Data; Right: Individual and Averaged Anatomic Dimensions for All Eight Subjects

	Coil	Transmit Phases (degree)								Body Geometry Dimensions (cm)[a]			
		k = 1	k = 2	k = 3	k = 4	k = 5	k = 6	k = 7	k = 8	A to P	L to R	A to C	P to C
Coil geometry[b]	1	0	25	65	90	180	205	245	270	—	—	—	—
Subject 1	1	0	133	180	52	213	243	45	267	17.7	30.0	7.1	10.5
Subject 2	1	0	70	188	52	139	172	308	287	16.8	32.0	8.0	8.8
										—	—	—	—
Coil geometry[b]	2	0	30	80	110	180	210	260	290	—	—	—	—
Subject 3	2	0	177	269	16	127	130	220	91	20.5	36.0	9.5	11.6
Subject 4	2	0	85	201	203	175	37	34	97	20.0	31.0	9.6	10.4
Subject 5	2	0	104	280	181	218	349	82	34	19.5	34.5	9.3	10.2
Subject 6	2	0	115	209	105	89	201	33	56	19.4	34.0	10.0	9.4
Subject 7	2	0	112	253	57	155	61	40	129	19.5	35.7	8.2	11.3
Subject 8	2	0	141	274	166	206	281	96	99	17.2	32.3	8.5	8.7
										18.8 ± 1.4	33.2 ± 2.2	8.8 ± 1.0	10.1 ± 1.1

[a] Anterior (A), posterior (P), left (L), right (R), center of prostate (C).

[b] Phases determined for each coil geometry assuming an anterior-posterior plate distance of 20 cm and a centrally localized focus.

Table 2

Left: B_1^+ Nonuniformity for Equal, Geometric, and B_1^+ Shim Phase Sets Generated from the Measured B_1^+ Magnitude Maps; Right: Measured Relative Transmit Efficiency (Measured RTE) in Comparison to Predicted Relative Transmit Efficiency (Predicted RTE)[a]

Subject	B_1^+ Mapping Flip Angles (degree)				B_1^+ Nonuniformity (%)c			Relative Transmit Efficiency (RTE)		
								Measured[d]		Predicted[e] Equal
	Nominal[b]	Equal	Geometric	B_1 Shim	Equal	Geometric	B_1 Shim	Equal	Geometric	
1	30	23.6 ± 7.6	—	53.5 ± 2.0	32	—	4	2.27	—	2.72
2	30	16.8 ± 5.7	—	52.9 ± 6.8	34	—	13	3.15	—	2.64
3	30	16.1 ± 8.2	—	146.7 ± 1.4	51	—	1	9.07	—	7.50
4	30	19.3 ± 5.0	—	38.8 ± 2.2	26	—	6	2.01	—	4.17
5	30	18.2 ± 7.6	26.7 ± 3.8	122.0 ± 7.8	42	14	5	6.70	4.57	5.80
6	45	24.1 ± 9.4	—	58.3 ± 3.7	39	—	6	2.42	—	2.54
7	60	—	32.7 ± 10.0	259.3 ± 5.9	—	30	2	—	7.92	7.58[f]
8	60	32.7 ± 11.5	37.9 ± 10.7	120.1 ± 4.8	35	28	3	3.67	3.17	3.23
					37 ± 8	24 ± 9	5 ± 4	4.2 ± 2.7	5.2 ± 2.4	4.5 ± 2.2

[a] Both nonuniformity and RTE measures were calculated from pixels within the optimization ROI which included the prostate.

[b] The lower nominal flip angle prescribed for B_1^+ magnitude mapping.

[c] B_1^+ nonuniformity defined as the standard deviation over the mean of flip angles measured within the optimization ROI for a given transmit phase set.

[d] Measured RTE defined as the average flip angle ratio between the B_1 shim phase and either equal phase or geometric phase.

[e] Predicted RTE defined as the MOS(post-shim)/MOS(pre-shim) averaged over the prostate.

[f] The only predicted RTE based on a geometric phase as the pre-shim value (i.e., RTE_g).